Catalytic removal of gaseous unintentional POPs on manganese oxide octahedral molecular sieves

Yang Yang, Jun Huang, Siwen Wang, Shubo Deng, Bin Wang, Gang Yu[*]

POPs Research Center, School of Environment, State Key Joint Laboratory of Environment Simulation and Pollution Control, Tsinghua University, Beijing 100084, China

ABSTRACT

Hexachlorobenzene (HCBz), pentachlorobenzene (PeCBz), and polychlorinated biphenyls (PCBs) are persistent organic pollutants emitted unintentionally from combustion and industrial processes. Catalytic removal of gaseous HCBz was achieved using manganese oxide octahedral molecular sieve (OMS) in four crystal structures: α-, β-, γ- and δ-MnO_2. All OMS catalysts present high activity at high space velocity (660,000 h^{-1}) in comparison to V_2O_5 based catalyst. The catalytic performance of OMS decreases in the order of δ- > α- > γ- > β-MnO_2. It is found that both adsorption and destruction processes influence the removal efficiency (RE). The former is positively correlated with surface area, pore (3.3–6.4 nm) volume, and surface acid sites, while the latter is coherent with both catalyst reducibility and the amount of surface labile oxygen. The best-performing δ-MnO_2 was further applied for the destruction of gaseous PeCBz, HCBz, and PCB mixture at trace concentration (305 $\mu g\,N\,m^{-3}$). High RE (99.3%) was achieved at 230 °C with the space velocity of 132,000 h^{-1}.

© 2013 Elsevier B.V. All rights reserved.

1. Introduction

Unintentional persistent organic pollutants (unintentional POPs) listed in the Stockholm Convention, including polychlorinated dibenzo-p-dioxin and dibenzofuran (PCDD/Fs), polychlorinated biphenyls (PCBs), hexachlorobenzene (HCBz), and pentachlorobenzene (PeCBz), are a group of hazardous organics emitted from combustion and several industrial processes [1–3]. The control strategies for PCDD/Fs, such as adsorption [4] and catalytic destruction [5], have been extensively studied. However, few attentions has been paid to the control of PeCBz, HCBz, and PCBs, while their emission concentration is much higher than that of PCDD/Fs [1–3].

Compared with adsorption, catalytic destruction shows a unique advantage due to the complete decomposition of hazardous organics. The vanadium-based catalysts (V_2O_5/TiO_2 or V_2O_5–WO_3/TiO_2) are widely adopted for the treatment of gaseous PCDD/Fs at 200–300 °C [6–8]. However, previous researchers have pointed out that it is less effective for the destruction of PeCBz, HCBz, and PCBs [9–12]. Therefore, it is necessary to develop novel catalysts with high destruction efficiency for all unintentional POPs.

In addition to VO_x, MnO_x is another group of catalysts with excellent oxidation activity. It is shown that MnO_x is inadequate for the treatment of chlorinated volatile organic compounds (Cl-VOCs)

at high concentration, as catalyst deactivation occurred gradually due to the strong binding between active sites and Cl atoms of Cl-VOCs [13]. However, it occurs to us that longer surface residence time may be benefited from such strong binding thereby promote the destruction efficiency of unintentional POPs at trace concentration. This speculation has been substantiated as high adsorption and destruction efficiency of PCDD/Fs were observed on Mn_3O_4 [14].

Depending on the linkage patterns of octahedral MnO_6 units, MnO_x can form four types of octahedral molecular sieve (OMS): α-, β-, γ- and δ-MnO_2 [15]. Their unique physicochemical properties have been extensively studied. For example, the tunnel structure of α-MnO_2 and layer structure of δ-MnO_2 both lead to high porosity and ion exchange ability [16,17]. The presence of surface oxygen vacancies on α- and γ-MnO_2 results in high reducibility [16,18,19].

Several environmental applications of OMS have been explored, high catalytic activity has been achieved on VOC oxidation [20–23], CO oxidation [24,25], and soot combustion [26]. Some researches further pointed out that the oxidation activity of δ-MnO_2 and α-MnO_2 is superior to that of Mn_3O_4, Mn_2O_3, and natural MnO_2 [21,26]. Therefore, OMS might be a group of promising catalysts for the treatment of unintentional POPs. However, to the best of our knowledge, no study published up to date has been focused on this scope.

In this paper, four types of OMS (α-, β-, γ- and δ-MnO_2) were synthesized. Their catalytic activities were studied based on the oxidative destruction of HCBz. With the aid of various characterization techniques, the catalyst structure-activity correlation was

* Corresponding author. Tel.: +86 10 62787137; fax: +86 10 62794006.
  E-mail address: yg_den@mail.tsinghua.edu.cn (G. Yu).

elucidated. We identified δ-MnO$_2$ with the highest HCBz adsorption capacity and destruction activity, and obtained successful results by applying δ-MnO$_2$ to simultaneously destruct PeCBz, HCBz, and PCB mixture.

2. Experimental

2.1. Chemicals

1,2,4,5-Tetrabromobenzene, HCBz, PeCBz, and 28 congeners of PCBs (PCB-8, 18, 28, 44, 52, 66, 77, 81, 101, 105, 114, 118, 123, 126, 128, 138, 153, 156, 157, 167, 169, 170, 180, 187, 189, 195, 206, 209) were analytical grade and obtained from Accustandard Co., USA. All chemicals were used as received without further purification. The PCB mixture covers di to deca-chlorinated homologues and 12 congeners of dioxin-like PCBs.

2.2. Catalysts preparation

α-, β-, γ-, and δ-MnO$_2$ were synthesized by hydrothermal method according to previous studies [24,27]. Briefly, δ-, α-, and β-MnO$_2$ were synthesized by the hydrothermal reaction between KMnO$_4$ and MnSO$_4$·H$_2$O. The crystalline phases were controlled by adjusting the Mn^{7+}/Mn^{2+} molar ratio and temperature. γ-MnO$_2$ was obtained by the hydrothermal reaction between MnSO$_4$·H$_2$O and (NH$_4$)$_2$S$_2$O$_8$. Detailed procedures are stated in Text S1 of supporting information.

Amorphous manganese oxide (denoted as AMO) and V$_2$O$_5$ (5 wt%)/WO$_3$–TiO$_2$ (denoted as VWTi) catalysts were chosen as reference catalyst. The former was obtained from Sinopharm Chemical Reagent, while the latter was provided by Zhong He Environmental Catalysis Corporation, China.

Prior the reaction, the catalyst powder was compressed into flakes with a hydraulic press, followed by crushing and subsequent sieving to 40–60 meshes (0.25–0.42 mm).

2.3. Catalysts characterization

Surface area, hydrogen temperature programmed reduction (H$_2$-TPR), ammonia temperature programmed desorption (NH$_3$-TPD), and oxygen temperature programmed desorption (O$_2$-TPD) analyses were conducted on Quantachrome Autosorb iQ gas sorption system:

(1) Surface area was obtained via N$_2$ adsorption at 77 K. Pore volume distribution was calculated based on non-local density functional theory (NLDFT), which is a more accurate model for the estimation of mesoporosity of molecular sieves compared with BJH model [28].
(2) Before H$_2$-TPR analysis, 50 mg catalyst was placed in U-shaped reaction tube, heated to 200 °C and purged with He for 1 h. After that, a mixture of 5% H$_2$/Ar (60 cm^3 min^{-1}) was purged into the reaction tube for TPR reaction. The temperature was increased at a rate of 10 °C min^{-1}, and the H$_2$ consumption was monitored by TCD detector.
(3) For NH$_3$-TPD analysis, 100 mg catalyst was loaded and pretreated in the same way of H$_2$-TPR. After that, the catalyst was purged with 10% NH$_3$/He at 100 °C. Desorption of NH$_3$ was carried out from 100 to 450 °C at a heating rate of 10 °C min^{-1} in He (60 cm^3 min^{-1}). This temperature was maintained for 1 h to achieve complete desorption.
(4) In the case of O$_2$-TPD analysis, 100 mg catalyst was heated to 150 °C and purged with He for 1 h to remove surface H$_2$O and physical adsorbed oxygen. After that, the catalyst was purged

with He and heated from 100 to 850 °C at a rate of 10 °C min^{-1}. The release of O$_2$ was monitored using TCD detector.

X-ray diffraction (XRD) analyses were done on D/MAX-RB (Rigaku) X-ray diffractometer with Cu Kα radiation. Surface element properties were analyzed by X-ray photoelectron spectroscopy (XPS) conducted on PHI-5300 electron spectrometer. The morphology of catalyst was observed on JSM-7401F field emission scanning electron microscope (FESEM).

2.4. Continuous reaction

The configurations of catalytic reactor and method for the generation of gaseous unintentional POPs have been described in our previous studies [29,30]. Briefly, target compounds were placed inside the heating chamber and gradually vaporized by elevating the temperature. For the activity and stability test, HCBz was vaporized alone, resulting in gas concentration of 7.6 ± 0.3 mg N m^{-3} (ca. 0.6 ppm). To determine the destruction activity of unintentional POPs, the mixture of PeCBz, HCBz, and 28 congeners of PCBs (100 ng of each compound was spiked on the quartz sand) were evaporated simultaneously to reach the total concentration of 305 ± 20 µg N m^{-3} (1.5 µg TEQ N m^{-3}). Vapor was purged into quartz reactor with 220 mL min^{-1} of carrier gas (10% O$_2$ and 90% N$_2$) and subsequent react with catalyst pellets at predetermined temperature. The pellets of OMS, AMO and VWTi have the same bulk density (ca. 1 g mL^{-1}). Therefore, 20 mg of catalyst pellet corresponds to the gas hourly space velocity (GHSV) of 660,000 h^{-1}.

For the short-term activity test (Section 3.2.1), the duration of reaction was set as 30 min. Off-gas sampling was started from the beginning of the reaction. Fresh catalyst was used in each run and triplicates were obtained at each temperature. In the case of adsorption experiment (Section 3.2.2) and stability test (Section 3.2.4), catalyst was continuously exposed to gaseous POPs for 10–10.5 h. The off-gas sampling was conducted at the interval of 120 min.

Accumulative gas sampling was employed in order to exceed the detection limit of GC–MS. Off-gas was successively scrubbed by acetone and hexane at 0 °C and the sampling period was set as 30 min. Two adsorptive solvents were then mixed, spiked with internal standard (1,2,4,5-tetrabromobenzene), followed by nitrogen sweeping and finally dissolved in 100 µL nonane prior GC–MS analysis. To determine the amount of residual reactant, catalyst was quenched at room temperature followed by ultrasonic extraction (twice by 15 mL hexane). The extracted solvent was concentrated by the same procedure described above. GC–MS analysis was performed on a Shimadzu QP2010 using a DB-5ms column (length: 30 m; film thickness: 0.25 µm). The GC oven temperature was set as follows: The initial oven temperature was set at 150 °C (held for 1 min), 20 °C min^{-1} to 210 °C, 2 °C min^{-1} to 245 °C (held for 2 min), 15 °C min^{-1} to 300 °C (held for 3 min). The temperature of injector, GC-MS interface and ion source were set as 270, 280, and 250 °C, respectively.

The removal efficiency (*RE*), adsorption efficiency (*AE*) and destruction efficiency (*DE*) are defined as follows:

$$RE\,(\%) = \frac{R_{in} - R_{out}}{R_{in}} \times 100 \tag{1}$$

$$AE\,(\%) = \frac{R_{cat}}{R_{in}} \tag{2}$$

$$DE\,(\%) = RE\,(\%) - AE\,(\%) \tag{3}$$

where R_{out} (µg) and R_{cat} (µg) are the amount of target compound collected by gas sampler and extracted from catalyst, respectively, and R_{in} (µg) is the amount of target compound in the inlet gas.
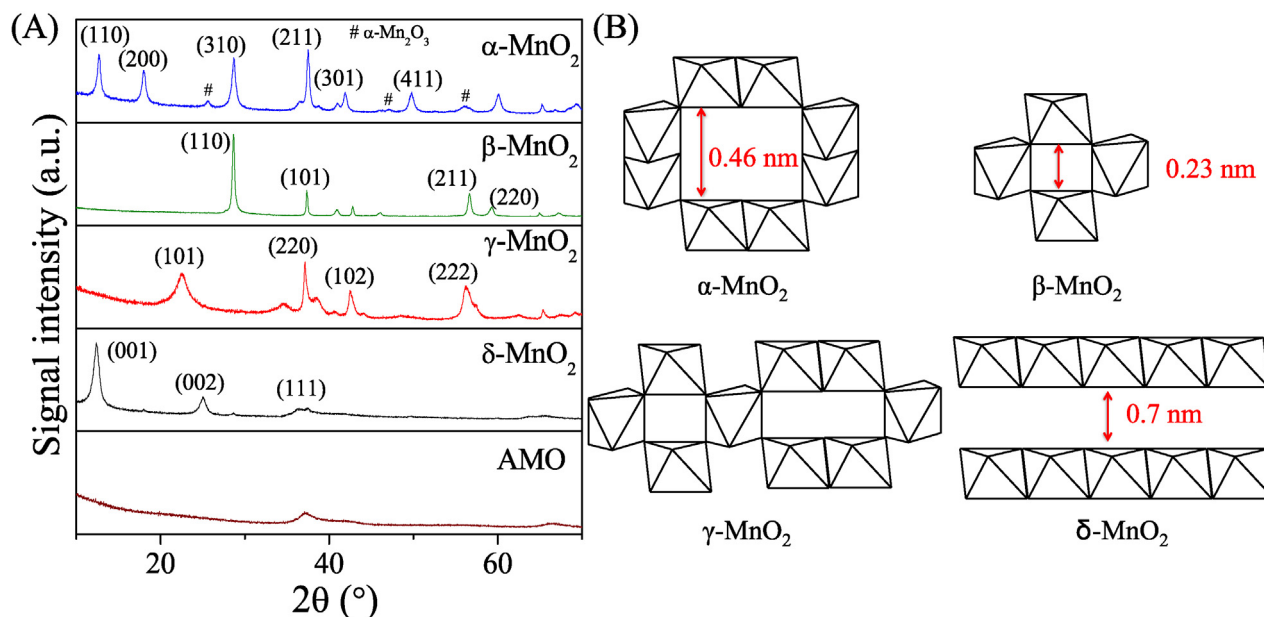
Fig. 1. (A) XRD profiles OMS and AMO and (B) different linkage pattern of MnO_6 units of OMS.

2.5. Batch reaction

The procedure of batch reaction has been described in previous studies [30,31]. 50 mg of catalyst was spiked with 2 mg of HCBz to reach a total HCBz concentration of 40 mg g^{-1}. The mixture was sealed with air in 25 mL glass ampules. According to the stoichiometric ratio calculated for the oxidative destruction reaction, oxygen was provided in excess to ensure the complete destruction of HCBz in the headspace of the sealed ampule. The ampules were placed in the furnace (preheated to 300 °C) to react for predetermined periods (10–40 min). After the reaction, the ampules were removed from the furnace and quenched at room temperature. For the analysis of residual HCBz and organic intermediates, ampules were crushed and the crude mixture was extracted with hexane, followed by GC–MS analysis. The selectivity of intermediates is calculated as follow:

$$\text{Selectivity}(\%) = \frac{iN_i}{6N} \times 100 \qquad (4)$$

where N_i is the molar mass of intermediate with i chlorine atoms in molecule. N is the molar mass of destructed HCBz. For the analysis of chloride (Cl$^-$), the ampules were extracted by 15 mL ultra pure water, followed by ionic chromatography analysis. The selectivity of Cl$^-$ is also calculated via Eq. (4).

3. Results and discussion

3.1. Catalyst characterization

3.1.1. XRD patterns, morphologies and textural properties

Fig. 1A shows the XRD profiles of synthesized OMS and commercial AMO. The diffraction peaks of α-, β-, γ-, and δ-MnO$_2$ can be well indexed to cryptomelane (JCPDS 29-1020), pyrolusite (JCPDS 24-0735), nsutite (JCPDS 17-0510), and birnessite (JCPDS 80-1098), respectively. The results show that most of the OMS were well crystallized and no impurity phase could be detected. As for α-MnO$_2$, the diffraction peaks of α-Mn$_2$O$_3$ (Bixbyite) were found at 23°, 46°, and 56°. According to previous study, four types of OMS correspond to different linkage patterns of MnO$_6$ octahedral unit [15]. That is, [2 × 2] for α-MnO$_2$, [1 × 1] for β-MnO$_2$, [1 × 1] + [1 × 2] intergrowth for γ-MnO$_2$, and layered structure for

δ-MnO$_2$ (Fig. 1B). The micro tunnel varies from 0.46 nm × 0.46 nm for α-MnO$_2$ to 0.23 nm × 0.23 nm for β-MnO$_2$, and the interlayer separation between MnO$_6$ sheets for δ-MnO$_2$ is 0.7 nm. No distinct peaks were found on the XRD pattern of AMO, implying the amorphous crystalline structure.

The morphologies of OMS and AMO were observed by FESEM. As shown in Fig. 2, OMS with α, β, and γ structure have nanorod morphology, while δ-MnO$_2$ presents microsphere shape and the layer structure in the corona expands perpendicularly from the core. The AMO exhibits irregular floc-like cluster, which is coherent with its amorphous crystalline structure.

Surface area (excluding micro tunnel area) of OMS was obtained by N$_2$ physisorption. The δ-MnO$_2$ with layer structure has the largest surface area (99 m^2 g^{-1}), followed by rod-like γ-MnO$_2$ (55 m^2 g^{-1}), α-MnO$_2$ (54 m^2 g^{-1}), and β-MnO$_2$ (13 m^2 g^{-1}). The commercial AMO adopted in this study has comparable surface area (68 m^2 g^{-1}). The mesopore structures of OMS and AMO were further investigated by NLDFT model. As shown in Fig. 3, the porosity of δ-MnO$_2$ is made up of uniform mesopores with diameters of 3.3–6.4 nm, which might be generated by the space between layer structures. Ambigious pore size distributions were observed on α-, β-, and γ-MnO$_2$, probably due to the irregularity generated by the random stack of nano-rods. The DFT plot of AMO also shows a narrow pore size distribution in the range of 3.3–4.3 nm. Moreover, the plot value increases with decreasing pore diameter in the range of 1–2 nm, indicating the existence of mesopores around 1–2 nm.

3.1.2. Acidic and redox properties

NH$_3$-TPD was adopted to evaluate the acidic properties of catalysts (Fig. 4). The area under the NH$_3$-TPD profile gives an estimation of the amount of acid sites and the peak position reveals binding strength between NH$_3$ molecule and acid sites. It seems that α- and δ-MnO$_2$ have many weak acid sites, while β-MnO$_2$ contains abundant strong acid sites. We also found that γ-MnO$_2$ and AMO have similar acid strength distribution, as two well-separated peaks were found in weak and strong acid region, respectively. Table 1 shows the quantitation of acid sites. AMO and γ-MnO$_2$ have the largest total acid amount, followed by δ-, α-, and β-MnO$_2$. It can be deduced that the amorphous structure of AMO and the
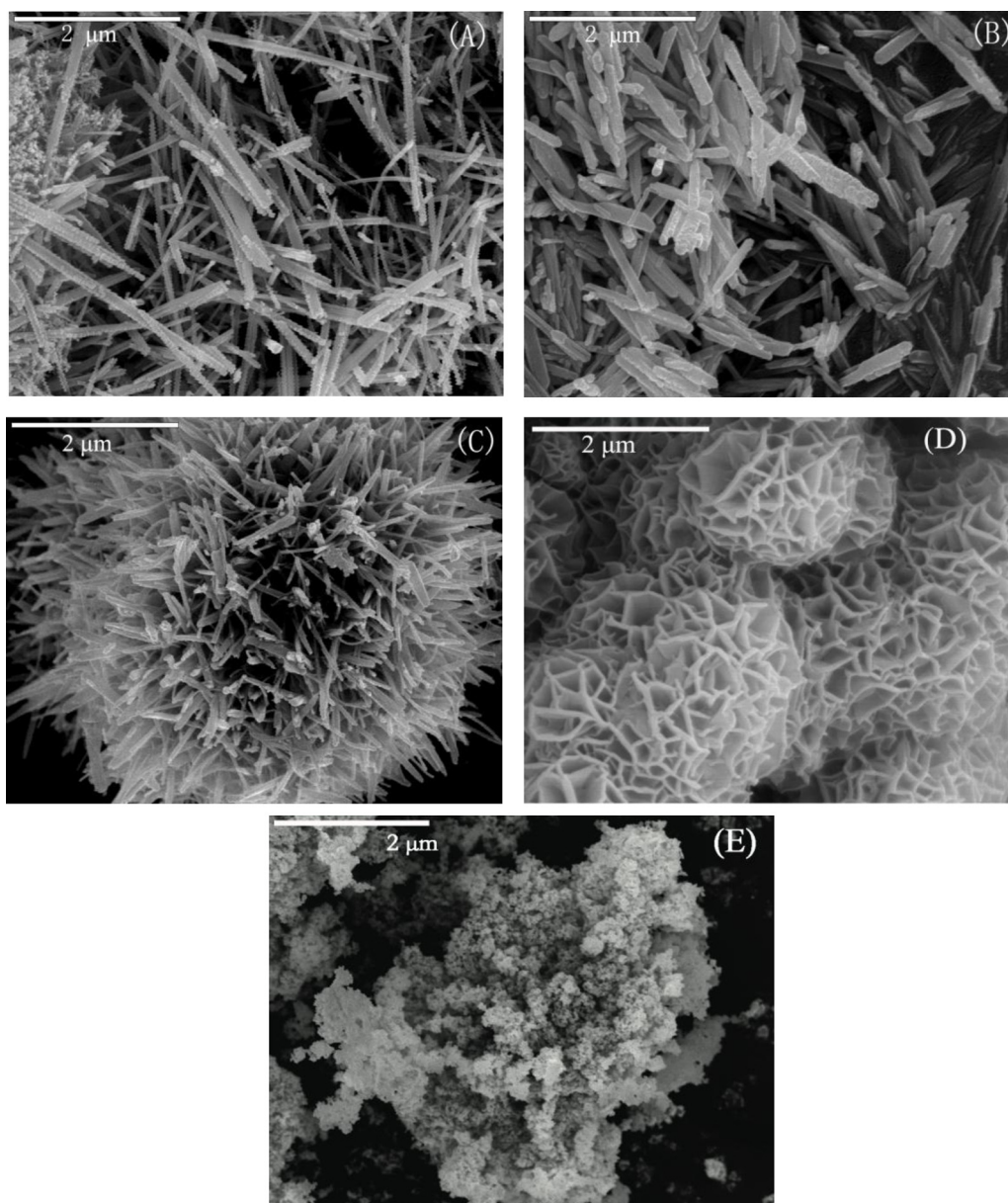
Fig. 2. FESEM images (A) α-, (B) β-, (C) γ-, (D) δ-MnO$_2$ and (E) AMO.

disordered linkage patterns of MnO$_6$ on γ-MnO$_2$ create lots of surface defect, which are responsible for the acidity.

The reducibility of catalysts was evaluated by H$_2$-TPR (Fig. 5A). For α-MnO$_2$, two reduction peaks were observed at 300 and 327 °C. The reduction pattern of δ-MnO$_2$ was similar to that of α-MnO$_2$, but the peak position shifted to lower temperature (276 and 314 °C). As for γ-MnO$_2$, the first reduction peak occurred at 302 °C while the second peak appeared at 394 °C. AMO exhibited similar reduction pattern to that of γ-MnO$_2$, with the first and second peak located at 300 and 393 °C, respectively. The reduction of β-MnO$_2$ seems to be difficult as the reduction peaks were observed at 520 and 557 °C. The first reduction peak at relative lower temperature could be attributed to the reduction of surface lattice oxygen (O$_{lat}$). With the further increase of temperature, successive bulk reduction occurs in the order of MnO$_2$ → Mn$_2$O$_3$ → Mn$_3$O$_4$ → MnO [24]. According to the position of the first reduction peak, the reducibility decreases in the order of δ-MnO$_2$ > α-MnO$_2$ > γ-MnO$_2$ ≈ AMO > β-MnO$_2$. Comparing with γ-MnO$_2$ and AMO, the reduction peaks of δ-MnO$_2$ and α-MnO$_2$ appeared in narrower window, implying the uniform bond
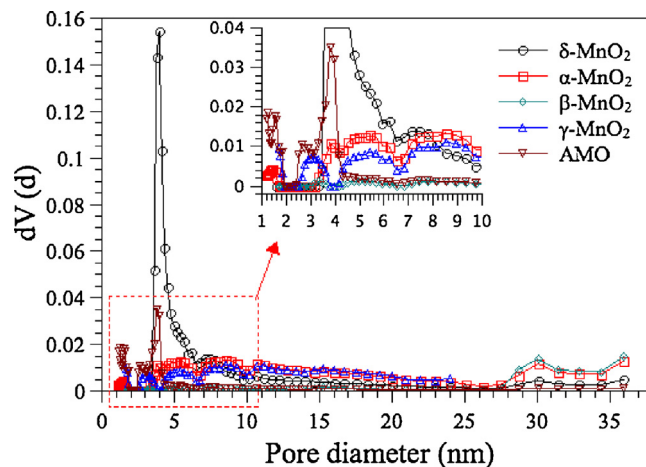

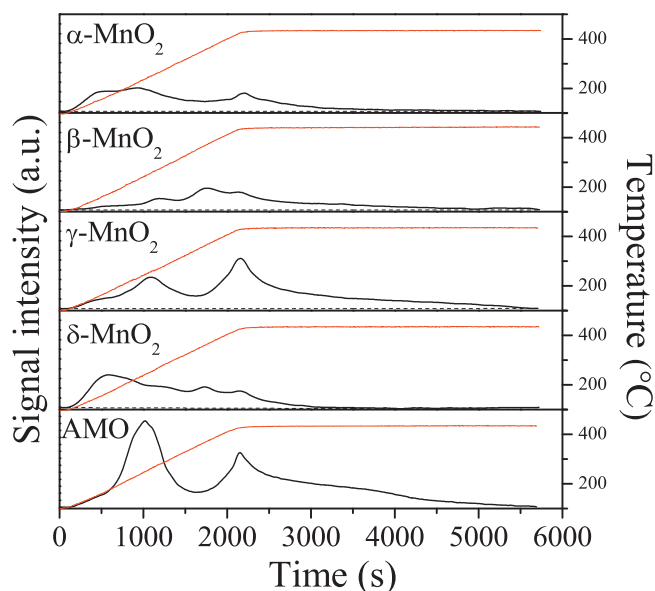**Fig. 3.** Pore size distribution of OMS and AMO based on NLDFT model.

Fig. 4. NH$_3$-TPD profiles of OMS and AMO.

Table 1
Acidic properties of OMS and AMO.

Catalyst	Total acidity (μmol NH$_3$ g^{-1})	Weak acidity (μmol NH$_3$ g^{-1})	Strong acidity (μmol NH$_3$ g^{-1})
α-MnO$_2$	661	391	270
β-MnO$_2$	566	107	459
γ-MnO$_2$	1191	367	824
δ-MnO$_2$	755	478	277
AMO	2572	1095	1477

energy of Mn—O and more active O$_{lat}$ available to react with H$_2$ at low temperature. Assuming MnO was the final reduction product, the bulk average oxidation state (AOS) of catalyst was calculated based on H$_2$ consumption (Table 2). It is found that the bulk AOS decreases in the order of β-MnO$_2$ (3.98) > γ-MnO$_2$ (3.73) > α-MnO$_2$ (3.60) $\approx$ δ-MnO$_2$ (3.57) > AMO (2.96).

The evolution of lattice oxygen was further investigated by O$_2$-TPD. As shown in Fig. 5B, the O$_2$-TPD spectra can be separated into

Table 2
Redox properties of OMS and AMO.

Catalyst	H$_2$ consumption (μmol g^{-1})	Bulk AOS	Evolution of lattice oxygen (μmol g^{-1})		
			Surface	Sub-surface	Bulk
α-MnO$_2$	9195	3.60	1088	317	953
β-MnO$_2$	11,264	3.98	90	3170	871
γ-MnO$_2$	9942	3.73	683	2526	1055
δ-MnO$_2$	9023	3.57	3042	153	705
AMO	5517	2.96	1136	2253	1067

three regions: low temperature (LT, <350 °C), medium temperature (MT, 350–650 °C), and high temperature (HT, >650 °C). The evolution of O$_2$ observed at LT corresponds to chemisorbed oxygen molecule and surface O$_{lat}$. The peaks at MT correspond to O$_{lat}$ released from the layer close to surface, and the peaks at HT can be assigned to the evolution of bulk O$_{lat}$. The evolution of O$_2$ is estimated by integrating the area of TPD curves, and the results are listed in Table 2. It is observed that the evolution of O$_{lat}$ on α-MnO$_2$ starts at 100 °C and continues above 650 °C. As reported by Liu et al. [16], the O$_{lat}$ of α-MnO$_2$ can be reversibly removed and recovered at the range of 100–650 °C without changing the framework structure. The O$_2$-TPD profile of δ-MnO$_2$ also exhibits two distinct O$_2$ desorption peaks located at LT and HT, and the evolution of surface O$_{lat}$ is more significant than bulk O$_{lat}$. Quantification results indicate that 46% and 78% of lattice O$_{lat}$ on α-MnO$_2$ and δ-MnO$_2$ are released at LT, implying these catalysts contain abundant loosely bound active O$_{lat}$. The evolution of O$_{lat}$ on γ-MnO$_2$ and AMO carried out in three well-separated stages, which is coherent with the separated reduction observed in H$_2$-TPR analysis. It can be deduced that the Mn—O bonds in γ-MnO$_2$ and AMO have different strength. In the case of β-MnO$_2$, the release of surface O$_{lat}$ at LT was negligible and the release of sub-surface and bulk O$_{lat}$ shifted to higher temperature comparing with other catalysts. This result is also in agreement with the poor reducibility observed in H$_2$-TPR analysis.

Oxygen that can be released from lattice or reduced by H$_2$ at LT is considered as labile oxygen species, which is highly active for the CO and benzene oxidation [16]. Here, the results of H$_2$-TPR and O$_2$-TPD indicate that both the activity of Mn—O bond and the amount of labile oxygen decrease in the order of
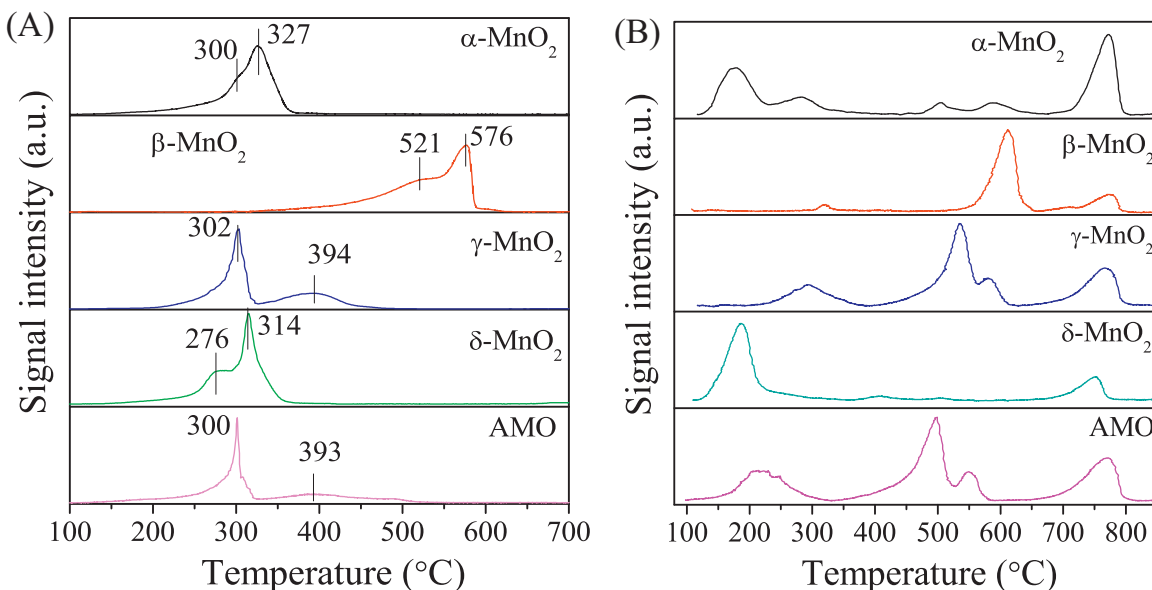

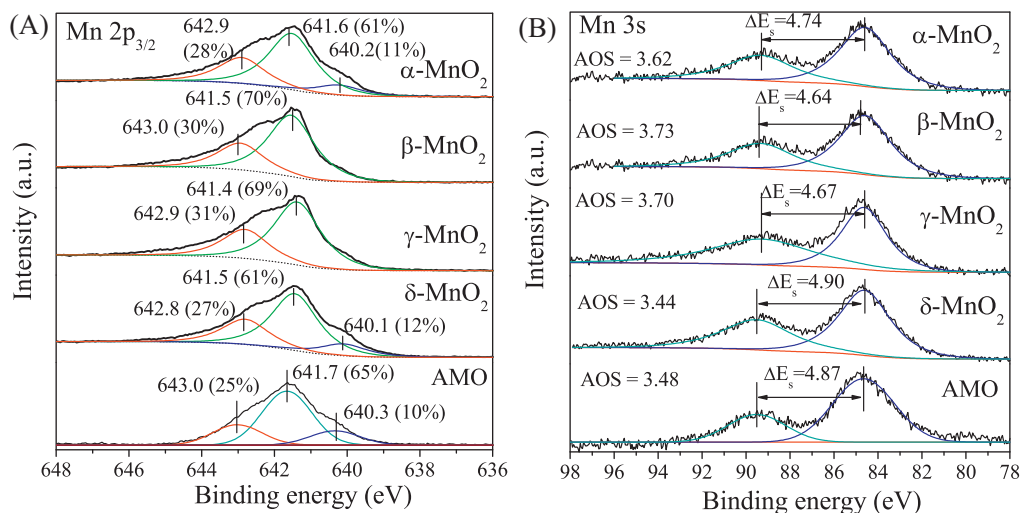**Fig. 5.** (A) H$_2$-TPR and (B) O$_2$-TPD profiles of OMS and AMO.

Fig. 6. High-resolution (A) Mn $2p_{3/2}$ and (B) Mn 3s XPS spectra of OMS and AMO.

δ- > α-MnO_2 > γ-MnO_2 ≈ AMO > β-MnO_2, which could be a prediction of catalytic performance in unintentional POPs oxidation.

3.1.3. Surface Mn state

Considering the fact that the activity of surface O_{lat} is determined by the Mn—O bond, it is necessary to investigate the surface Mn state via XPS. The relative abundance of surface Mn species for AMO and each OMS was calculated by obtaining the high resolution Mn $2p_{3/2}$ XPS spectra (Fig. 6A). The Mn $2p_{3/2}$ peak can be deconvoluted into three peaks with binding energy of 640, 641, and 643 eV attributed to Mn^{2+}, Mn^{3+} and Mn^{4+} [18], respectively. It is observed that Mn^{3+} is the dominant species on both OMS and AMO, followed by Mn^{4+}. Distinct peaks around 640 eV were found on the high-resolution Mn $2p_{3/2}$ XPS spectra of δ-MnO_2, α-MnO_2, and AMO, indicating the existence of Mn^{2+} species.

The surface AOS of Mn was estimated based on the formula [32,33]: $AOS = 8.956 - 1.126 \Delta E_s$, where ΔE_s is the BE of the doublet separation of Mn 3s peaks (Fig. 6B). The results show that the AOS decreases in the order of β-MnO_2 (3.73) > γ-MnO_2 (3.70) > α-MnO_2 (3.62) > AMO (3.48) > δ-MnO_2 (3.44). The relative low surface AOS of α-MnO_2, δ-MnO_2, and AMO further confirms the existence of Mn species in lower valance, i.e. Mn^{2+}. The results suggest that the presence of surface Mn^{2+} creates surface labile oxygen on α-MnO_2, δ-MnO_2, and AMO. On one hand, the bond energy of Mn(II)—O is weaker than that of Mn(III)—O and Mn(IV)—O, which facilitates the release of oxygen. On the other hand, due to the difference of electronegativity between Mn^{2+} (1.43) and Mn^{4+} (1.95) [34], the mobility of oxygen in Mn(II)—O—Mn(IV) bridge might be promoted by the electronic delocalization effect.

3.2. Catalytic removal of HCBz

3.2.1. Activity test

Previous lab-scale studies usually adopt high concentration (100–1000 ppm) mono- or di-chlorobenzene as model compound. In this study, HCBz was chosen as a surrogate, as HCBz has the highest resistance to the oxidative destruction among unintentional POPs [10,35]. In real flue gas, the concentrations of HCBz are in the range of 7–200 μg N m^{-3} [1,3]. In this study, the inlet HCBz concentration was set at 7.6 ± 0.3 mg N m^{-3} (ca. 0.6 ppm) to approach the real condition. Moreover, in order to amplify the diversity of catalytic activity, the reaction was conducted at high GHSV (660,000 h^{-1}).

Prior the activity test, blank test was conducted on non-porous quartz sand. It is shown that HCBz was neither homogeneously destructed at 300 °C nor physically condensed at 180 °C. Fig. 7A presents the RE of HCBz as a function of temperature. In
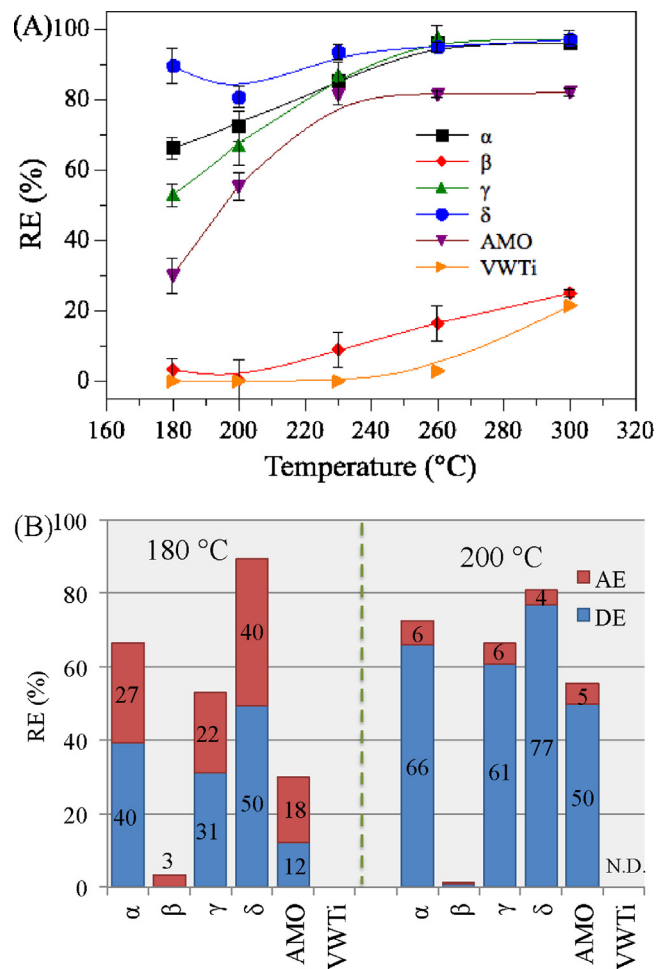

Fig. 7. (A) Removal efficiency and (B) adsorption/destruction efficiency of HCBz on fresh OMS, AMO and VWTi catalysts (inlet HCBz concentration: 7.6 mg N m^{-3}; GHSV: 660,000 h^{-1}; catalyst amount: 20 mg).

general, the RE increases with increasing temperature in the region of 180–300 °C. The activity of OMS decreases in the order of δ- > α- > γ- > β-MnO$_2$. δ-MnO$_2$ presents the best performance as the RE maintained above 80% in all investigated temperatures. AMO is less active than most of the OMS, and its activity was limited when temperature exceeded 230 °C. Compared with MnO$_x$, the commercial VWTi catalyst, which showed high HCBz destruction activity at 5000 h^{-1} in our previous study [30], did not work well at high GHSV.

Neither chlorine balance nor carbon balance could be established in activity test due to the low inlet concentration. However, GC-MS analysis showed that only un-destructed HCBz were detected in concentrated adsorptive solvent while no other chlorinated by-products could be detected, indicative of the deep destruction of HCBz. As will be shown later, the chlorine atoms in destructed HCBz could be recovered as chloride (Cl$^-$) in batch reaction. Therefore, the end-products are suspected to be HCl and CO$_x$.

The analysis of residual HCBz on catalyst after reaction shows that part of the RE was contributed by adsorption when temperature was below 200 °C (Fig. 7B). At 180 °C, δ-MnO$_2$ showed the highest AE, followed by α-MnO$_2$, γ-MnO$_2$, AMO, and β-MnO$_2$. The AE decreased and DE increased when the temperature increased to 200 °C. It seems that high temperature is adverse to the adsorption, but facilitates the destruction reaction. When temperature was higher than 230 °C, the RE equals to DE since no HCBz was removed via adsorption. As for VWTi, neither adsorption nor destruction of HCBz could be observed at 180–230 °C. It seems that the removal of HCBz is determined by both adsorption and destruction. Therefore, these steps are separately investigated in Sections 3.2.2 and 3.2.3.

3.2.2. Adsorption of gaseous HCBz under inert environment

The catalysts were exposed to continuous HCBz stream under inert environment. After the breakthrough was achieved, the residual HCBz on catalyst was analyzed, and the adsorption capacity was normalized to a per-gram basis (mg g^{-1}). As illustrated in Fig. 8A, δ-MnO$_2$ presents the highest adsorption capacity at 180 °C, followed by α-MnO$_2$, AMO, γ-MnO$_2$, and β-MnO$_2$. This tendency matches with the trend of changes in AE observed in Fig. 7B. As reported previously, surface acid sites of metal oxides were considered as the adsorptive sites for Cl-VOC such as chlorobenzene [36] and dichloroethane [37,38]. However, in this study, AMO with the largest acid amount did not exhibit the highest HCBz adsorption capacity. The explanation of this conundrum may lie within the physical properties of reactants. Because the boiling point of HCBz (322 °C) is significantly higher than that of Cl-VOC, the adsorption of HCBz on OMS might be mainly controlled by physical process rather than the chemical interaction between molecule and acid sites.

Seemingly, the HCBz adsorption capacity at 180 °C is related to the surface area. δ-MnO$_2$ with the largest surface area exhibits the highest adsorption capacity while β-MnO$_2$ with the lowest surface area shows the lowest adsorption capacity. However, the adsorption behaviors of α-MnO$_2$, γ-MnO$_2$, and AMO do not fit this tendency, implying that other factors need to be taken into account.

According to previous study, the adsorption of small molecule, such as CO [24], CO$_2$ [39], and NH$_3$ [40,41], is depended on the micro tunnels of OMS (shown in Fig. 1B). However, due to its large molecular diameter (0.93 nm), HCBz cannot enter those micro tunnels. Hence, the physical adsorption is mainly determined by the mesopore structure. Considering the fact that δ-MnO$_2$ with the highest HCBz adsorption capacity also has narrow pore distribution around 3.3–6.4 nm, those pore structures might be critical to physical adsorption. A linear relationship between the pore (3.3–6.4 nm) volume and HCBz adsorption capacity on OMS and AMO substantiates our speculation (Fig. 8B). Due to its high boiling point, the
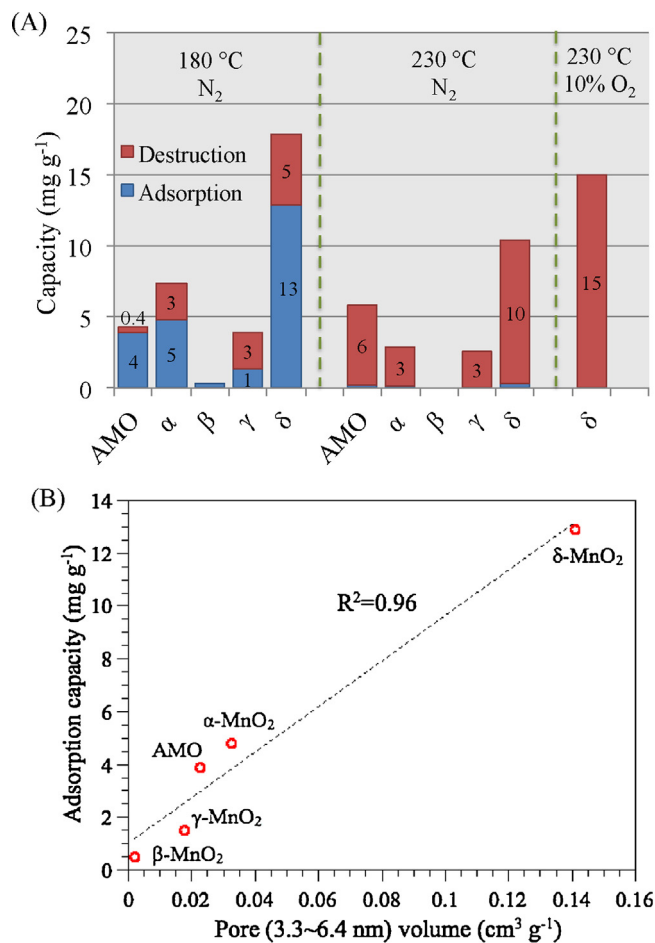

Fig. 8. (A) Adsorption and destruction capacity measured under inert environment; (B) correlation between adsorption capacity and pore volume at 180 °C (inlet HCBz concentration: 7.6 mg N m^{-3}; GHSV: 660,000 h^{-1}; catalyst amount: 20 mg; equilibrium time: 600 min).

gaseous HCBz at 180 °C is suspected to be in the form of aerosol particles, which may have diameter greater than single molecule. These aerosols can be accommodated by the mesopores around 3.3–6.4 nm and subsequently captured via capillary condensation mechanism.

To evaluate the adsorption strength, reactant-TPD techniques were widely adopted [42]. Unfortunately, the HCBz-TPD cannot be performed due to the absence of online monitoring apparatus (conventional online mass spectrometer is inappropriate to analyze HCBz at low concentration with large molecular weight). Instead, the adsorption strength was investigated by measuring the HCBz adsorption capacity at 230 °C. The results show that the adsorption of HCBz on α-MnO$_2$, γ-MnO$_2$, and β-MnO$_2$ was negligible, while the adsorption capacity of δ-MnO$_2$ and AMO dramatically reduced to 0.3 and 0.23 mg g^{-1}, respectively. Since the chemisorption has stronger binding than physisorption. It can be deduced that the effect of physisorption was weaken at the elevated temperature, while the effect of chemisorption became increasingly dominant, leading to similar adsorption capacity of δ-MnO$_2$ and AMO.

Although the reaction was conducted in the absence of oxygen, the destruction of HCBz was observed on both OMS and AMO at 180 °C. The results show that O$_{lat}$ was involved in the destruction of HCBz under inert environment. The destruction capacity increased as temperature increased to 230 °C, probably due to the enhanced activity of O$_{lat}$. In the presence of 10% O$_2$, the destruction capacity of δ-MnO$_2$ was further promoted to 15.0 mg g^{-1} (data is obtained from long-term reaction in Section 3.2.4). These data suggest that

the oxidation of HCBz on OMS followed the Mars van Krevelen mechanism. That is, the adsorbed HCBz was first oxidized by the O_{lat} of OMS and then the consumed O_{lat} was replenished by gas phase O_2. Similar mechanism has been reported on the oxidation of CO [16,24] and toluene [18] catalyzed by OMS.

Neither adsorption nor destruction of HCBz was observed for VWTi catalyst (data not shown), implying that the VWTi has lower adsorptivity for HCBz compared with OMS. VWTi has moderate surface area ($49\,m^2\,g^{-1}$) but the pore volume around 3.3–6.4 nm is substantially less ($0.011\,cm^3\,g^{-1}$), resulting in weaker physisorption of HCBz. In addition, the comparison of NH_3-TPD plots (Fig. S1) shows that VWTi has less acid sites than OMS, implying fewer coordination sites for chemical adsorption of HCBz. Moreover, the nature of VO_x and MnO_x may also affect the surface-HCBz binding. For the VWTi catalyst adopted in this study, the VO_x is responsible for the adsorption of HCBz as the VO_x is highly dispersed on WO_3–TiO_2 (proved in our previous study [30]) and the coverage exceeds monolayer (calculation is based on surface area and cross-section area of VO_x [43]). MnO_x was reported to have stronger binding affinity to chlorine atom than VO_x in the dissociative adsorption of HCl in Deacon reaction [44]. Therefore, such strong binding might also exist between the chlorine atoms in HCBz molecule and OMS.

3.2.3. Batch reaction

In batch reaction, the effect of mass transfer was minimized, because catalyst was pre-spiked with HCBz and the reaction was conducted in sealed system. Therefore, each catalyst has the same HCBz concentration and residence time on their surface. As illustrated in Fig. 9A, the residual HCBz on catalyst decreases with increasing reaction time. Apparently, the HCBz destruction on δ-MnO_2 occurs the fastest, followed by α-, γ-, and β-MnO_2. After 20 min, the destruction reaction catalyzed by α- and γ-MnO_2 became retard, implying the deactivation of catalyst. Surprisingly, δ-MnO_2 seems to be less affected by Cl-poisoning, as the retard of reaction was ambiguous and all the HCBz were destructed within 40 min.

For unbiased comparison, the surface destruction rates of all catalysts were calculated within the linear region (the initial 10 min), which were 9.9 for δ-MnO_2, 7.5 for α-MnO_2, 4.7 for γ-MnO_2, 4.5 for AMO, and $0.14\,\mu mol\,min^{-1}\,g^{-1}$ for β-MnO_2. It is found that the surface destruction rate is correlated with the amount of surface labile oxygen (Fig. 10). Thereby, it suggests that the active sites in HCBz oxidative destruction are associated to the labile oxygen species in interaction with the low-coordinated Mn atoms of the oxide structure. Moreover, the surface acid site is not the limited factor as AMO merely exhibited moderate reaction rate. The results suggest that δ-MnO_2 not only has high adsorption capacity but also has the fastest surface destruction rate, which might be the reason of its outstanding performance in activity test.

The batch reaction catalyzed by VWTi has been reported in our previous research [30]. By comparison, the VWTi has similar surface destruction rate with α-MnO_2 (Fig. 9A). This finding highlights again the importance of adsorptivity. It seems that the low activity of VWTi in continuous reaction is not due to the low surface destruction rate, but rather the low adsorptivity of HCBz. Weaker adsorption of HCBz means HCBz has shorter residence time on catalyst surface, which is adverse to the catalytic destruction [10,45].

Reaction pathway was investigated by intermediate analysis. Although no intermediate was detected in continuous reaction, trace amount of di- to penta-chlorinated benzene and hexachlorobutadiene (C_4Cl_6) were detected as intermediates in batch reaction catalyzed by δ-, α-, and γ-MnO_2 (quantitative results are demonstrated in Tables S1–S3). PeCBz was identified as the major intermediate. As shown in Fig. 9B, the selectivity of PeCBz reaches
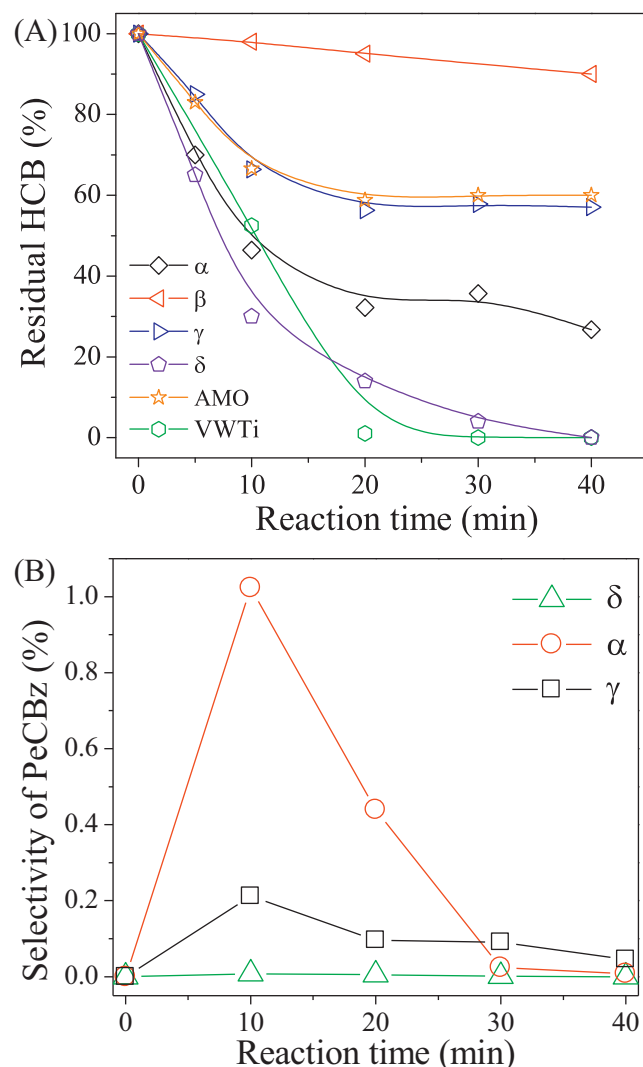
Fig. 9. (A) Residue amount of HCBz and (B) selectivity of PeCBz in batch reaction (dose of HCBz: 2 mg; catalyst amount: 50 mg; temperature: 300 °C).

maximum value (1%) at 10 min and then gradually decreases with the increasing reaction time.

It is suspected that the dissociation of C–Cl bond is the initial step of HCBz destruction on OMS. In the presence of proton donor
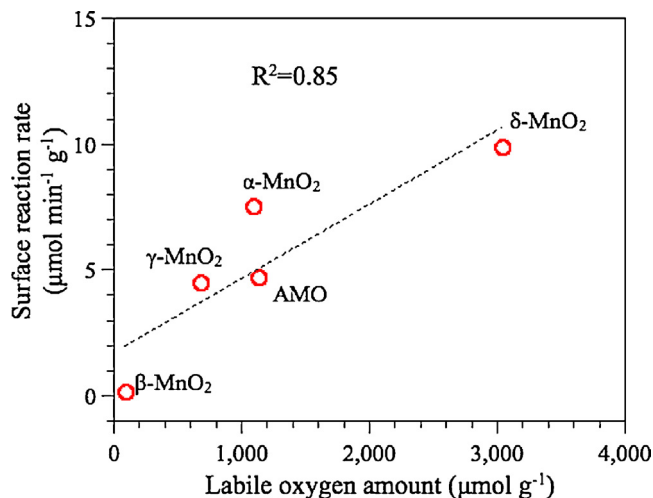
Fig. 10. Correlation between labile oxygen amount and surface destruction rate.
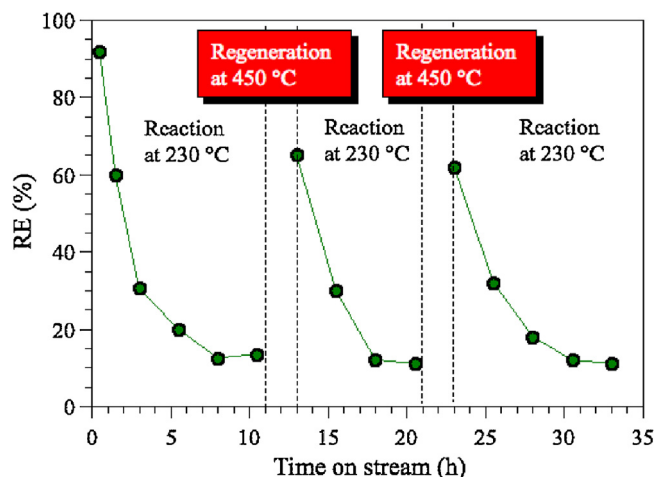
Fig. 11. Long-term HCBz destruction reaction catalyzed by δ-MnO$_2$ (HCBz concentration: 7.6 mg N m^{-3}; GHSV: 660,000 h^{-1}; catalyst amount 20 mg).

(surface hydroxyl on α-, γ-, and δ-MnO$_2$ [24]), HCBz was protonated to PeCBz and other lower chlorinated benzenes. C$_4$Cl$_6$ was detected at 30 and 40 min of the reaction catalyzed by α- and γ-MnO$_6$, indicative of the subsequent oxidative ring opening. Intermediates could be barely detected on δ-MnO$_2$, which is another indication of the fast destruction rate. After 40 min reaction, Cl mass balance was established. The selectivity of inorganic chloride (Cl$^-$) was 103% for the reaction catalyzed by δ-MnO$_2$, 95% for α-MnO$_2$ and 99% for γ-MnO$_2$, while the selectivity of organic chloride was negligible (<0.1%). These results further confirm the deep destruction of HCBz on OMS.

3.2.4. Deactivation and regeneration

The δ-MnO$_2$ was identified with highest catalytic destruction activity and was selected to test its stability. The long-term reaction was conducted at 230 °C, 660,000 h^{-1} (Fig. 11). Although δ-MnO$_2$ proved to be stable in CO oxidation [24], the gradual deactivation during HCBz oxidation was observed. The RE dropped gradually from 90% to 10% after 10.5 h of reaction.

XRD analysis (Fig. 12A) indicates that the spent catalyst (obtained after 10.5 h of reaction) remained as δ-MnO$_2$ structure and no peaks corresponding to MnCl$_x$ were observed, suggesting that the deactivation was not due to the bulk phase transformation. The formation of KCl was identified, probably due to the reaction between inorganic end-products (HCl or Cl$_2$) and K$^+$ originated from interlayer of δ-MnO$_2$. XPS analysis indicates a surface Cl atomic concentration of 2.6%, implying the partial chlorination of catalyst surface. As indicated by Liang et al. [24], the stable performance of δ-MnO$_2$ for CO oxidation is associated with the fast replenish of consumed surface O$_{lat}$ from gas phase O$_2$. Here, the surface reaction mechanism of HCBz destruction is more complicated: after the cleavage of benzene structure, the chlorine atoms may form complex with surface Mn, forming less active MnO$_y$Cl$_z$ species [13,46]. O$_2$-TPD characterization of the spent catalyst (Fig. 12B) shows the decrease of the amount of surface labile oxygen after long-term reaction. It seems that the surface Cl impeded the regeneration of consumed surface O$_{lat}$, resulting in the reduction of active sites.

To coupe with the deactivation, δ-MnO$_2$ was subjected to aerobic re-oxidation at 450 °C for 2 h as the liberation of surface Cl from MnO$_2$ is an endothermic reaction [44]. After regeneration, the surface Cl atomic concentration of δ-MnO$_2$ reduced to 1.5% (obtained from XPS analysis) and no phase transformation was observed from XRD pattern (Fig. 12A). Meanwhile, O$_2$-TPD analysis (Fig. 12B) shows that the amount of surface labile oxygen was
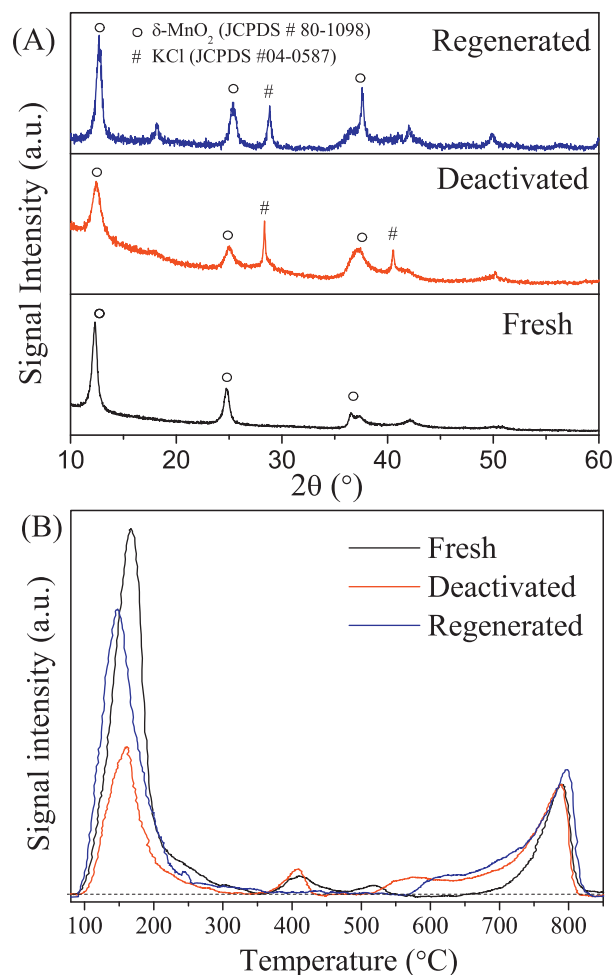

Fig. 12. (A) XRD profiles and (B) O$_2$-TPD plot of deactivated and regenerated δ-MnO$_2$.

partially recovered after regeneration. The activity test of regenerated δ-MnO$_2$ (Fig. 11) shows that the RE of HCBz recovered to 60% and the regeneration was reproducible after two cycles of deactivation. The incomplete regeneration of activity is probably due to the reduction of surface area (from 99 m^2 g^{-1} to 68 m^2 g^{-1}) and the incomplete removal of surface Cl. Further study focused on the surface Cl removal at lower temperature via surface modification of δ-MnO$_2$ are currently under way.

3.3. Catalytic removal of PeCBz, HCBz and PCBs

δ-MnO$_2$ was adopted to dispose the mixture of PeCBz, HCBz, and PCBs at trace concentration (305 ± 20 µg N m^{-3}). As illustrated in Fig. 13A, δ-MnO$_2$ shows high activity for HCBz, PeCBz, and PCBs. 97.7% of unintentional POPs was removed (83.4% by destruction and 14.3% by adsorption) at 200 °C and 132,000 h^{-1}. The adsorption of PCBs indicates that the pore structure of δ-MnO$_2$ is also capable of capturing POPs with molecular diameter larger than that of HCBz. The AE of di- to octa-CB increased with increasing chlorinated degree, implying that the adsorption capacity is reversely correlated with volatility. However, nona- and deca-CB with the lowest volatility were mainly removed by destruction, probably due to two reasons: (1) the nona- and deca-CB have the longest residence time on δ-MnO$_2$, thereby facilitating the destruction; (2) as the destruction is initiated by the cleavage of C—Cl, their high chlorinated structure provides more possible cleavage sites. The inlet
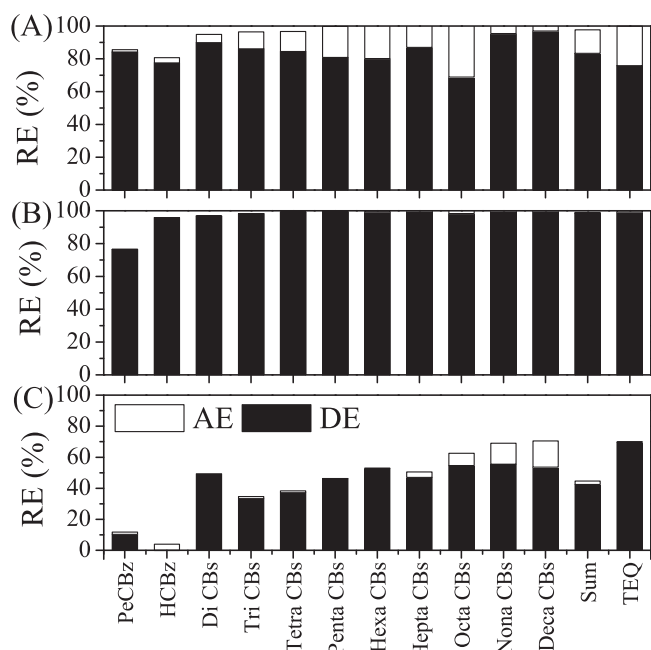
Fig. 13. Destruction/adsorption efficiency of unintentional POPs on δ-MnO$_2$ at (A) 200 °C, (B) 230 °C and on (C) VWTi at 200 °C (inlet concentration: 305 ± 20 μg N m^{-3}; GHSV: 132,000 h^{-1}; catalyst amount: 100 mg).

PCB mixtures contained 12 congeners of dioxin-like PCBs, resulting in an inlet concentration of 1.5 μg TEQ N m^{-3}. The results show that these highly toxic compounds could be effectively removed by δ-MnO$_2$ via destruction and adsorption, resulting in the RE of 99.99% (based on TEQ concentration).

When the temperature was raised to 230 °C (Fig. 13B), 99.3% of unintentional POPs were removed by destruction (98.6%) and adsorption (0.7%). The RE of PCBs is 99.3% and 99.5% calculated by mass concentration and TEQ concentration, respectively. HCBz and PeCBz were mainly removed by destruction and the contribution of adsorption was negligible.

The reaction catalyzed by VWTi catalyst was also operated at 200 °C and 132,000 h^{-1} (Fig. 13C). It is proved again that the δ-MnO$_2$ catalyst presents enhanced reactivity comparing with VWTi catalyst, as VWTi catalyst is less effective for the removal of PCBs and incompetent for the removal of PeCBz and HCBz.

In addition, since PeCBz and HCBz are considered as the surrogates of PCDD/Fs in catalytic research [35], it is reasonable to speculate that δ-MnO$_2$ is potentially effective for the destruction of PCDD/Fs. Therefore, we believe that δ-MnO$_2$ is a promising catalyst for the disposal of unintentional POPs at low concentration.

4. Conclusion

Four types of OMS (α-, β-, γ-, and δ-MnO$_2$) were synthesized by hydrothermal method and characterized by various physicochemical techniques. Their activities for unintentional POPs removal were evaluated. The following conclusions can be drawn:

(1) OMS catalysts are effective for gaseous HCBz removal. The performance decreases in the sequence of δ- > α- > γ- > β-MnO$_2$. The high RE is contributed by both adsorption and catalytic destruction.
(2) The adsorption of HCBz is affected by both physical and chemical process. The former is dominated by surface area and pore volume around 3.3–6.3 nm; the latter is depended on surface acidity.

(3) The destruction of HCBz is positively correlated with the amount of surface labile oxygen. The regeneration of surface labile oxygen via Mars van Krevelen mechanism is the rate-limiting step, which can be hindered by surface chlorine deposition after long-term reaction.
(4) δ-MnO$_2$ shows enhanced activity for the removal of the mixture of PeCBz, HCBz, and PCBs comparing with VWTi catalyst, which makes it a promising catalyst for the removal of gaseous unintentional POPs at low concentration.

Appendix A. Supplementary data

Supplementary data associated with this article can be found, in the online version, at http://dx.doi.org/10.1016/j.apcatb.2013.05.048.

References

[1] E. Wikstrom, M. Tysklind, S. Marklund, Environmental Science and Technology 33 (1999) 4263–4269.
[2] B. Tian, J. Huang, B. Wang, S. Deng, G. Yu, Chemosphere 89 (2012) 409–415.
[3] M. Watanabe, Y. Noma, Journal of Environmental Science and Health, Part A. Toxic/Hazardous Substances and Environmental Engineering 45 (2010) 846–854.
[4] K. Everaert, J. Baeyens, Waste Management 24 (2004) 37–42.
[5] E. Finocchio, G. Busca, M. Notaro, Applied Catalysis B: Environmental 62 (2006) 12–20.
[6] M.B. Chang, K.H. Chi, S.H. Chang, J.W. Yeh, Chemosphere 66 (2007) 1114–1122.
[7] S.H. Chang, K.H. Chi, C.W. Young, B.Z. Hong, M.B. Chang, Environmental Science and Technology 43 (2009) 7523–7530.
[8] R. Weber, M. Plinke, Z.T. Xu, M. Wilken, Applied Catalysis B: Environmental 31 (2001) 195–207.
[9] T. Sakurai, R. Weber, S. Ueno, J. Nishino, M. Tanaka, Chemosphere 53 (2003) 619–625.
[10] R. Weber, T. Sakurai, H. Hagenmaier, Applied Catalysis B: Environmental 20 (1999) 249–256.
[11] P. Liljelind, J. Unsworth, O. Maaskant, S. Marklund, Chemosphere 42 (2001) 615–623.
[12] R. Weber, T. Sakurai, Applied Catalysis B: Environmental 34 (2001) 113–127.
[13] F. Bertinchamps, C. Poleunis, C. Grégoire, P. Eloy, P. Bertrand, E.M. Gaigneaux, Surface and Interface Analysis 40 (2008) 231–236.
[14] H.C. Wang, S.H. Chang, P.C. Hung, J.F. Hwang, M.B. Chang, Journal of Hazardous Materials 164 (2009) 1452–1459.
[15] Q. Feng, H. Kanoh, K. Ooi, Journal of Hazardous Materials 9 (1999) 319–333.
[16] J. Luo, Q. Zhang, J. Garcia-Martinez, S.L. Suib, Journal of the American Chemical Society 130 (2008) 3198–3207.
[17] D. Golden, J. Dixon, C. Chen, Clays and Clay Minerals 34 (1986) 511–520.
[18] V.P. Santos, M.F.R. Pereira, J.J.M. Orfao, J.L. Figueiredo, Applied Catalysis B: Environmental 99 (2010) 353–363.
[19] L. Lamaita, M.A. Peluso, J.E. Sambeth, H.J. Thomas, Applied Catalysis B: Environmental 61 (2005) 114–119.
[20] R.H. Wang, J.H. Li, Environmental Science and Technology 44 (2010) 4282–4287.
[21] F. Wang, H. Dai, J. Deng, G. Bai, K. Ji, Y. Liu, Environmental Science and Technology 46 (2012) 4034–4041.
[22] L. Jin, C.H. Chen, V.M.B. Crisostomo, L.P. Xu, Y.C. Son, S.L. Suib, Applied Catalysis A-General 355 (2009) 169–175.
[23] A.R. Gandhe, J.S. Rebello, J.L. Figueiredo, J.B. Fernandes, Applied Catalysis B: Environmental 72 (2007) 129–135.
[24] S.H. Liang, F.T.G. Bulgan, R.L. Zong, Y.F. Zhu, Journal of Physical Chemistry C 112 (2008) 5307–5315.
[25] W.Y. Hernández, M.A. Centeno, S. Ivanova, P. Eloy, E.M. Gaigneaux, J.A. Odriozola, Applied Catalysis B: Environmental 123–124 (2012) 27–35.
[26] I. Atribak, A. Bueno-López, A. García-García, P. Navarro, D. Frías, M. Montes, Applied Catalysis B: Environmental 93 (2010) 267–273.
[27] X. Wang, Y. Li, Chemistry: A European Journal 9 (2003) 300–306.
[28] P.I. Ravikovitch, A.V. Neimark, Journal of Physical Chemistry B 105 (2001) 6817–6823.
[29] Z. Xu, S. Deng, Y. Yang, T. Zhang, Q. Cao, J. Huang, G. Yu, Chemosphere 87 (2012) 1032–1038.

[30] Y. Yang, G. Yu, S. Deng, S. Wang, Z. Xu, J. Huang, B. Wang, Chemical Engineering Journal 192 (2012) 284–291.
[31] Y. Fan, X. Lu, Y. Ni, H. Zhang, L. Zhao, J. Chen, C. Sun, Environmental Science and Technology 44 (2010) 3079–3084.
[32] V.P. Santos, M.F.R. Pereira, J.J.M. Orfao, J.L. Figueiredo, Topics in Catalysis 52 (2009) 470–481.
[33] V.P. Santos, O.S.G.P. Soares, J.J.W. Bakker, M.F.R. Pereira, J.J.M. Órfão, J. Gascon, F. Kapteijn, J.L. Figueiredo, Journal of Catalysis 293 (2012) 165–174.
[34] Y. Zhang, Inorganic Chemistry 21 (1982) 3886–3889.
[35] J.E. Lee, J. Jurng, Catalysis Letters 120 (2008) 294–298.
[36] E. Finocchio, G. Ramis, G. Busca, Catalysis Today 169 (2011) 3–9.
[37] B. de Rivas, C. Sampedro, M. García-Real, R. López-Fonseca, J.I. Gutiérrez-Ortiz, Applied Catalysis B: Environmental 129 (2013) 225–235.
[38] B. de Rivas, R. López-Fonseca, J.R. González-Velasco, J.I. Gutiérrez-Ortiz, Journal of Molecular Catalysis A: Chemical 278 (2007) 181–188.

[39] L. Espinal, W. Wong-Ng, J.A. Kaduk, A.J. Allen, C.R. Snyder, C. Chiu, D.W. Siderius, L. Li, E. Cockayne, A.E. Espinal, S.L. Suib, Journal of the American Chemical Society 134 (2012) 7944–7951.
[40] C. Wang, L. Sun, Q. Cao, B. Hu, Z. Huang, X. Tang, Applied Catalysis B: Environmental 101 (2011) 598–605.
[41] Z.-M. Wang, S. Tezuka, H. Kanoh, Catalysis Today 68 (2001) 111–118.
[42] H.C. Genuino, S. Dharmarathna, E.C. Njagi, M.C. Mei, S.L. Suib, Journal of Physical Chemistry C 116 (2012) 12066–12078.
[43] F. Bertinchamps, C. Gregoire, E.M. Gaigneaux, Applied Catalysis B: Environmental 66 (2006) 1–9.
[44] M.W.M. Hisham, S.W. Benson, Journal of Physical Chemistry 99 (1995) 6194–6198.
[45] K. Everaert, J. Baeyens, Journal of Hazardous Materials 109 (2004) 113–139.
[46] Y. Liu, M.F. Luo, Z.B. Wei, Q. Xin, P.L. Ying, C. Li, Applied Catalysis B: Environmental 29 (2001) 61–67.